ACS APPLIED MATERIALS & INTERFACES
Research Article
www.acsami.org

Superhydrophobic Surfaces as Smart Platforms for the Analysis of Diluted Biological Solutions

Francesco Gentile,*[†,‡] Maria Laura Coluccio,[†] Nicola Coppedè,[§] Federico Mecarini,[†] Gobind Das,[‡] Carlo Liberale,[‡] Luca Tirinato,[‡] Marco Leoncini,[‡] Gerardo Perozziello,[†] Patrizio Candeloro,[†] Francesco De Angelis,[‡] and Enzo Di Fabrizio[†,‡]

[†]BioNEM Laboratory, Department of Experimental and Clinical Medicine, University Magna Graecia of Catanzaro, Catanzaro, 88100 Italy

[‡]Nanostructures Department, Italian Institute of Technology, Via Morego 30, Genova, 16163 Italy

[§]IMEM-CNR Parco Area delle Scienze 37/A, Parma, 43124 Italy

Ⓢ *Supporting Information*

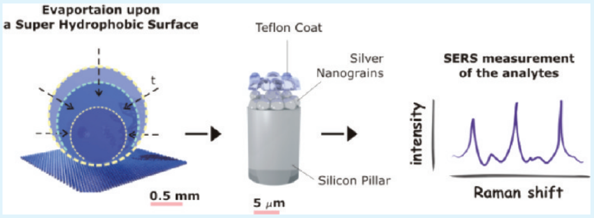

ABSTRACT: The aim of this paper is to expound on the rational design, fabrication and development of superhydrophobic surfaces (SHSs) for the manipulation and analysis of diluted biological solutions. SHSs typically feature a periodic array or pattern of micropillars; here, those pillars were modified to incorporate on the head, at the smallest scales, silver nanoparticles aggregates. These metal nanoclusters guarantee superior optical properties and especially SERS (surface enhanced Raman scattering) effects, whereby a molecule, adsorbed on the surface, would reveal an increased spectroscopy signal. On account of their two scale-hybrid nature, these systems are capable of multiple functions which are (i) to concentrate a solution, (ii) to vehicle the analytes of interest to the active areas of the substrate and, therefore, (iii) to measure the analytes with exceptional sensitivity and very low detection limits. Forasmuch, combining different technologies, these devices would augment the performance of conventional SERS substrates and would offer the possibility of revealing a single molecule. In this work, similar SHSs were used to detect Rhodamine molecules in the fairly low atto molar range. The major application of this novel family of devices would be the early detection of tumors or other important pathologies, with incredible advances in medicine.

KEYWORDS: *superhydrophobic surfaces, SERS, biophotonic devices, single molecule detection, cancer*

1. INTRODUCTION

Nanotechnology is a new science concerned with the study and the fabrication of devices whose size is, in at least a dimension, comprised in the nanometer range.[1] These systems deliver the promise of changing the way biomedical sciences are practiced, in that they feature characteristic length scales that are of the same order of magnitude of biological objects (from cells, as large as ten micrometers, to biomolecules sizing a few nanometers or less) and can accordingly interact with these in a fashion that new physical/biological laws, strategies, or possibilities emerge.[2] Examples where nanotechnologies are applied to biology include, for instance, surfaces patterned with random, rather than periodic, micro- nano- fabricated themes, to guide cell attachment and proliferation;[3,4] micro- nano-fabricated needles, holes, or fluidic channels for transdermal drug administration, protein sorting, and cell analysis;[5,6] microstuctured, three-dimensional scaffolds for tissue engineering;[7] nanoparticles for the smart delivery of drugs and/or imaging contrast agents;[8,9] devices for molecular detection, identification, and diagnosis. Molecular sensors comprise a variety of different systems, including nanowires and nano-cantilevers, microarrays,[10] and nanoporous silicon surfaces, where the species of interest can be selectively adsorbed and detected using MALDI TOF mass spectroscopy techniques.[11]

The detection of few, small molecules, and with that the recognition of a disease, is particularly important in the case of cancer and other pathologies, in that the early stages of disease are typically treated with the greatest probability of success.[12,13] Albeit the large variety of systems mentioned above, surface enhanced Raman scattering (SERS) substrates are the most promising in terms of sensitivity, reproducibility, and reliability.[14] These nanogeometry based devices are capable of detecting biological moieties in the limits of very low abundance ranges, thus offering the most effectual way for the detection of a single molecule.

SERS is a phenomenon whereby the electromagnetic field, at the close proximity of metal nanoclusters, is locally enhanced because of the resonant interaction with the surface plasmons in the metal.[14,15] Surface plasmons are collective oscillations of conduction electrons and can get excited by the light of a laser beam. Those plamons, in turn, then radiate a dipolar field that

Received: March 29, 2012
Accepted: May 23, 2012
Published: May 23, 2012

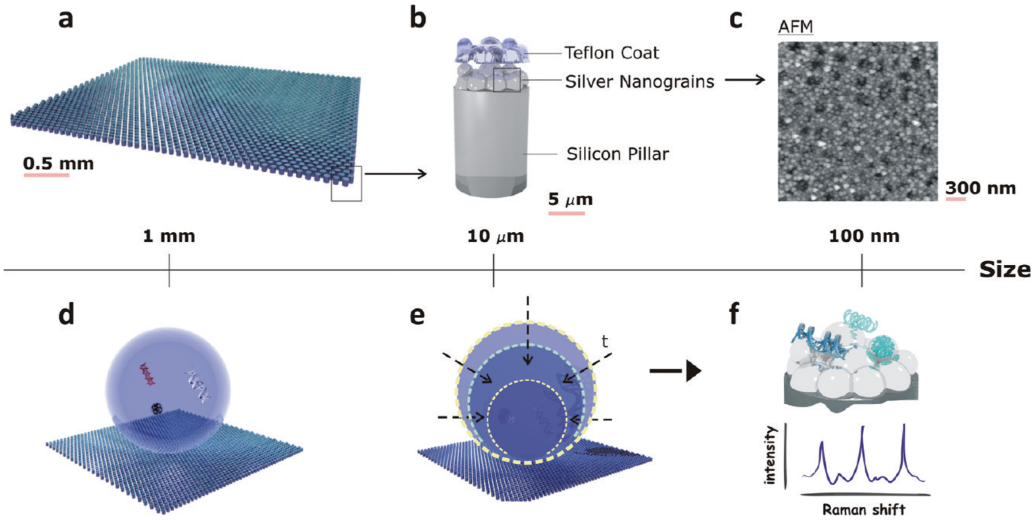

Figure 1. The device features hierarchically different scales in correspondence of which different functions are revealed. On a large scale, the superhydrophobic substrate looks continuous, millimetric drops are repelled, and solutions can be easily manipulated (a,d). On a mesoscale, that is micrometric, micropillars (b) permit the evaporation of the solution whereby the solute is concentrated into a small area (b,e). On a nanoscale, silver nanoparticles assemblies, positioned upon the pillars (c), induce SERS effects and permit the identification of analytes in the single molecule regime (f).

leads to a redistribution of electric field intensities. A molecule, adsorbed on the metal nanocluster, would thus feel an increased field intensity, and its Raman spectroscopy signal would be accordingly amplified. Thus, the ingredients for SERS are basically two, that is, (i) features at the nanoscale and (ii) the presence of metals, especially gold, silver, or copper.

Recent advances in nanofabrication techniques fostered the invention and development of even more performing SERS devices, such as periodic, regular arrays of metal nanodots;[14] adiabatic nanofocusing cones;[16,17] or nanolenses, which are groups of three hierarchical metal hemispheres, where the diameters of the spheres or, equivalently, their distances, are in a perfect ratio.[18] Interestingly, random rough surfaces, with a roughness in a nanometric scale, also exhibit superior sensing capabilities[19] but, differently from regular geometries, they retain the advantages of short fabrication times. In 2008, Coluccio et al. devised a SERS sensor constituted by silver nanonanoparticles aggregates, where the metal grains were formed using an electroless deposition technique.[20] Electroless growth is a process that is capable to attain extreme control over the key characteristics of the nanoparticles aggregates, such as shape and size, at the smallest scales, and this would guarantee the conditions for the most correct functioning of SERS; in the method, metal ions are reduced and deposited as metals upon a silicon surface.

Despite the extremely high enhancement factors that are achievable *in theory*, SERS substrates generally suffer from a practical and serious limitation, that is, the huge time that the species of interest would take to reach and interact with the active sites of the substrate. In a solution at rest and under the effect of diffusion solely, a biomolecule with a Brownian diffusion coefficient $D = 10^{-9}$ m^2/s would take some 60 h to travel the distance of 1 cm, that is the typical length side of the device. Thus, the performance of conventional, bidimensional SERS substrates would be dramatically limited by the bottleneck of diffusion.

Here, electroless grown, nanogeometry based photonic devices, as those described above in the text, were integrated with superhydrophobic surfaces (SHSs) to overcome the limit of diffusion. By doing so, novel multifunctional systems were obtained with high selectivity, resolution, and very low detection limits. SHSs are artificial, micro- or nanofabricated surfaces, with a texture given by a regular array of cylindrical pillars. The top of the pillars was conveniently modified to incorporate random assemblies of silver nanograins (Figure 1). In sight of a dramatically low friction coefficient, this innovative family of devices offers realistic possibilities for the detection of extremely low concentrated solutions of analytes, and this discloses terrific opportunities in medicine. A mathematical description of SHSs was provided, on the basis of which the devices were designed and fabricated; extremely diluted biological solutions were therefore analyzed. Rhodamine molecules were detected in the very low abundance range of 10^{-18} M.

1.1. Description of the Principle.

Small drops of deionized water, containing the moieties at study, are positioned upon the substrate and let it evaporate. In sight of a simple balance of forces, the line of contact at the solid interface would therefore recede with time, and thus, the footprint of the drop would also gradually be reduced. When the drop gets sufficiently small (where "small" is defined on the basis of a mathematical criterion described in the Section 2.3 below and depends on the geometry and surface chemistry of the substrate), a transition to a more stable state occurs, whereby the drop is firmly attached to the substrate, and the scale-down of the area of contact is prevented. Thereupon, few molecules would be accumulated in a very small region, assuring an increased density and, accordingly, the attainment of the limits of detection (Figure.1).

2. THE MODEL

Nature has endowed the leafs of some plants with the noticeable capability of repelling water, whereby a drop, positioned upon those leaves, would assume a shape that resembles that of a sphere.[21] Surfaces that exhibit a behavior like this are superhydrophobic. The most practical property of SHSs is a reduced friction coefficient in virtue of which they can be used for a number of different applications, including, on the

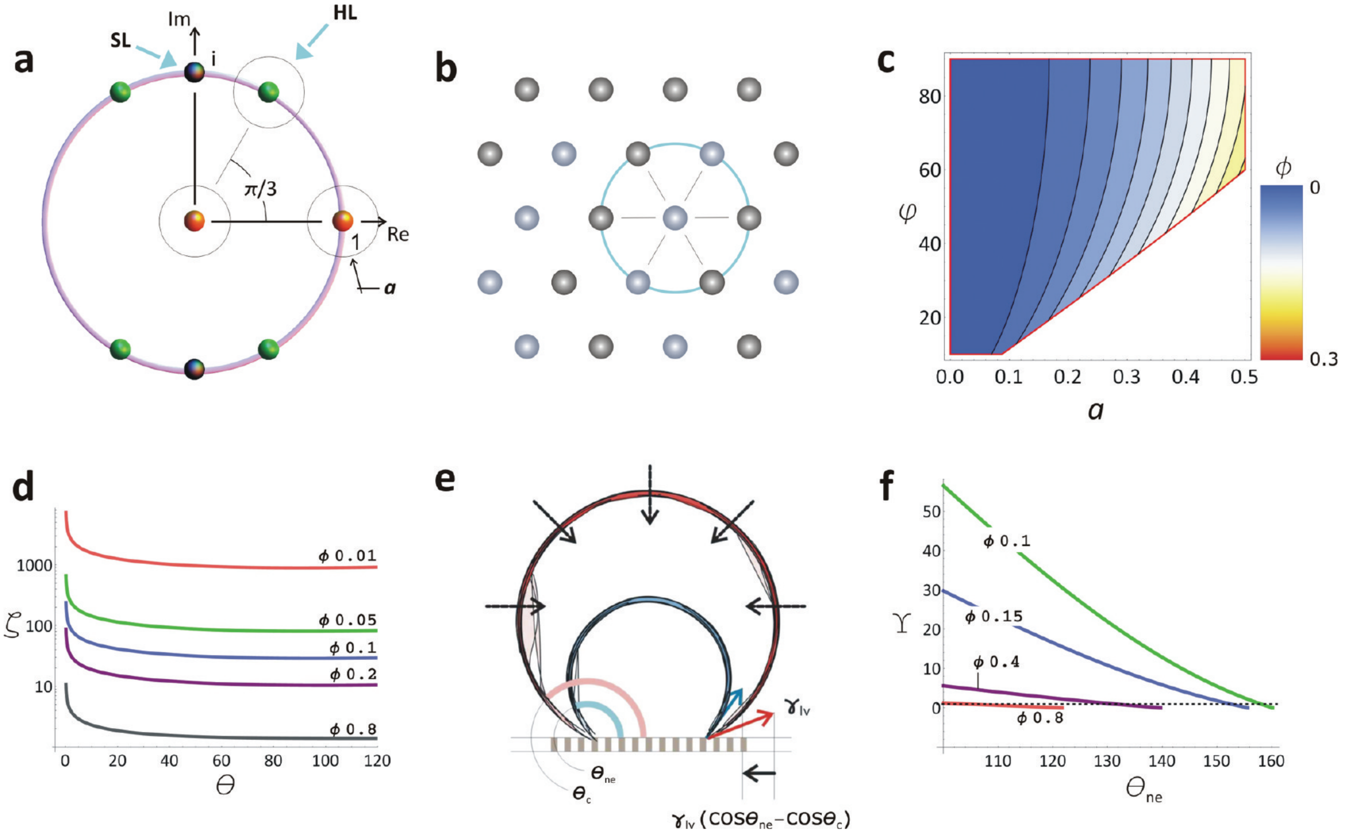

Figure 2. Representation of lattices in the complex plane (a). The hexagonal lattice has, in the plane, the largest coordination number $n = 6$ (b). Contour plot of the solid fraction ϕ as a function of the nondimensional pillars' diameter a and of the angle φ that defines the lattice orientation (c). The augmented ability of a drop to slide over a textured surface ($\phi < 1$) with respect to a continuous, flat surface ($\phi = 1$), as a function of the equilibrium contact angle θ (d). Cartoon representing the evaporation process over a textured surface (e). The nondimensional force Υ that pushes the contact line inward during evaporation, as a function of the nonequilibrium contact angle θ_{ne} (f).

medical side, the manipulation and control of diluted solutions of biological interest.[22,23] SHSs typically feature two distinguishing ingredients and, namely, (i) a quasi periodic hierarchical structure with dimensions comprised in the micro- to nanometer range (and thus the geometry) and (ii) a superficial, chemical, or physical, modification of the surface. Understanding the mechanisms whereby the combination of these ingredients reduces wettability is essential for the rational design of artificial SHSs. In the following paragraphs, the laws describing the wetting phenomena are briefly recapitulated (I); it is explained why a hexagonal lattice of pillars would mimic natural SHSs better than other configurations (II). The dynamics of slowly evaporating droplets, and the influence of certain parameters thereon, are discussed (III); and last, the parameters describing the lattice above are optimized on the basis of a mathematical criterion (IV).

2.1. The Physics of Drops and Surfaces. It is well-known that the physics of micrometric or submillimetric drops is correctly governed by surface tension solely (Supporting Information #1). The angle of contact θ at the solid/air/liquid interface indicates the propensity of a droplet of whether wetting or not a surface. Surfaces where $\theta > 150°$ are superhydrophobic. Interestingly, perfectly flat surfaces may have, via chemical modifications, a contact angle that is 120° at most.[24] Artificial superhydrophobic states are possible solely for those surfaces which incorporate a regular pattern or texture.[25] Superhydrophobic states are very well described by the models of Wenzel[26] and Cassie–Baxter.[27] In 1936, Wenzel explained the increased contact angle θ_w in terms of geometrical effects only and especially as a function of the solid roughness r (r is the real interfacial area over projected area, and it is always larger than one),

$$\cos\theta_w = r\cos\theta \tag{1}$$

and thus the effect of surface roughness is to amplify the wetting. Differently from Wenzel, Cassie explained superhydrophobicity on account of the pockets of air that remain trapped between the drop and the substrate; in particular, he expressed the augmented contact angle θ_c as

$$\cos\theta_c = -1 + \phi(\cos\theta + 1) \tag{2}$$

where ϕ is the fraction of solid in contact with the drop (and notice that ϕ is always smaller than one). The lower ϕ, the larger is the apparent contact angle. At the limit of $\phi \to 0$, the drop would paradoxically float in air. The Cassie model is intuitive in that it predicts that a drop, upon a patterned surface, develops a contact angle that is proportional to the fraction of air in contact with the drop. These models are very different from their adhesive properties: while Wenzel drops are strongly pinned, in the Cassie state the drop sits mainly upon air, and this improves the self-cleaning properties of the surface. On comparing eqs 1 and 2, one can notice that a drop configuration would transition from Cassie to Wenzel, provided that the following identity holds:

$$\cos(\theta) = \left(\frac{\phi - 1}{r - \phi}\right) \tag{3}$$

Eq 3 claims that the Cassie state is assured if the contact angle θ of the flat, not-modified material is sufficiently large, that is, larger than a certain, nonlinear combination of the geometrical parameters of the substrate (Supporting Information #2). The Cassie state, and thus the nonwetting behavior of the surface, would be assured if ϕ is sufficiently large or, equivalently, if the pillars that constitute the surface are sufficiently dense.[25,28] Notice though that large ϕ would induce small contact angles, and thus, the choice for the best parameters in eq 3 is not trivial; it is indeed a matter of optimization. Equation 3 holds on average: situations are reported in literature where the Cassie configuration holds despite a small ϕ, meaning that it is a *metastable* state. Practically, this means that, if positioned with sufficient care upon a surface, a drop would not collapse even if it is supposed to, in that an energy barrier inhibits the spontaneous transition of the droplet to the level of lower energy content.[29,30]

2.2. Lattice Packings and SHSs. Here, the mathematical representation of lattices is introduced. This is important because SHSs can be artificially reproduced by a discrete subset of cylindrical micropillars, whose centers are placed in the plane as to recover a 2-dimensional (2D) lattice. In brief, we translate the problem from being expressed in terms of the sole ϕ to a geometrical, more intuitive, form, where parameters such as the pillars' diameter or gap have a clear significance and can be easily manipulated in a fabrication process.

A point lattice Λ, in a bidimensional space, is a regularly spaced array of points. The mathematical form of Λ is

$$\Lambda = \{\sum_{i=1}^{D} a_i \nu_i | a_i \in \mathrm{Z}\} \tag{4}$$

where $D = 2$ is the number of Euclidean dimensions that the lattice fills and $\{\nu_1, \nu_2\}$ is a basis for $\mathbf{R}^2$. Every lattice in $\mathbf{R}^2$ is completely determined given the fundamental parallelotope, that is the region of the plane that would reproduce the original lattice by simple translations. The fundamental parallelotope is thus the elementary cell therefrom the whole space can be reconstructed. Its volume is uniquely determined by Λ, and the square of this volume is called determinant of the lattice.[31] Here, the representation of 2D lattices in a complex plane is discussed. A lattice is defined by a pair of unit vectors, consider the first of these vectors being $\nu_1 = (1,0)$ or, in a complex notation, simply $\nu_1 = 1$. The position of the second vector in the plane is thus sufficient for describing the geometry of the entire lattice. The circumference in Figure 2a describes all the configurations that are isotropic, where with isotropic we define a lattice with the same internodal distances in the ν_1 and ν_2 directions. Thus, for instance, a regular square pattern is the complex number $\nu_2 = \mathbf{i} = e^{i\pi/2}$ (where $\mathbf{i}$ is the imaginary unit and the celebrated Euler formula has been used), while a hexagonal lattice would be lumped in the sole number $\nu_2 = e^{i\pi/3}$. In the realm of this structure, the multiplication of a lattice by another holds the meaning of a rotation, and thus, for instance, $e^{i\pi/2} \times e^{i\pi} = e^{i3\pi/2}$, and notice that $e^{i3\pi/2}$ is still a square lattice. Considering that, with Conway et al.,[31] the area of the parellotope can be written as the determinant of the generator matrix $\mathbf{M} = [\nu_1, \nu_2]$, for the present configuration it follows that

$$A_p^{\ 2} = \det\Lambda = (\det M)^2 = \begin{vmatrix} \nu_{11} & \nu_{12} \\ \nu_{21} & \nu_{22} \end{vmatrix}^2 = \begin{vmatrix} 1 & 0 \\ \cos\varphi & \sin\varphi \end{vmatrix}^2 = \sin^2\varphi \tag{5}$$

where the first of the pair of unit vectors that describe the lattice is hold constant, being $\nu_1 = (1,0)$, while the second is left free to rotate by an arbitrary angle φ, being $\nu_2 = (\cos\varphi, \sin\varphi)$, and thus the determinant of the lattice is the square of the imaginary part of ν_2. The consequence of this is that the diagram of Figure 2a finds a direct interpretation, that is, all the points that are equally distant from the real axis describe the same pattern. For instance, $e^{i\pi/3}$, $e^{i2/3\pi}$, $e^{i4/3\pi}$, and $e^{i5/3\pi}$ are equivalent and all represent the hexagonal lattice (Figure 2b). This representation may be of some help in deriving ϕ as a function of the architecture of the pillars, as explained below.

Consider an isotropic periodic array of cylinders. Let the diameter of these cylinders be d, their distance, or pitch, instead, p. If we divide d by p, we obtain a variable, a, that is comprised between 0 and 1. When $a = 0$, the cylinders are vanishingly small, when $a = 1$, the cylinders would get in contact. Being now nondimensional, the cylinder diameter a can be reported in the diagram of Figure 2a and, in doing so, we immediately see that the solid fraction ϕ can be derived as the ratio of the area of one pillar, to the area A_p of the fundamental parallelotope, $\phi = \pi/2^2\, a^2/A_p = \pi/2^2\, a^2/\sin\varphi$.

The contourplot in Figure 2c reports ϕ as a function of a and φ, and the smaller a, or the larger φ, the smaller is ϕ. The diagram thus suggests that small pillars, organized in nonslanted geometries, are superhydrophobic. The white region of the diagram describes geometries which are not realizable (impossible geometries) in that, there, the pitch would be smaller than the diameter of the pillars, and these would therefore interfere. Notice that ϕ varies with a to a much more extent than with φ, and this would suggest that it is important to choose a with accuracy (using a mathematical criterion as explained later in the text). Hexagonal tilings are preferred (and have been used in this work) in that they are optimal in the sense that they solve the (i) densest packing and (ii) highest kissing number problems in the plane.[31] The kissing number (or coordination number) n is the number of circles, in 2 dimensions, which can touch an equivalent circle without any intersections. It is important because large kissing numbers would guarantee that the distances between a pivot pillar and the neighboring ones is the same, and thus, the problem is highly symmetric. For a hexagonal lattice, $n = 6$.

2.3. Vanishingly Small Friction Coefficients of SHSs and Evaporation Dynamics. Consider a drop sitting upon a surface and experiencing an arbitrary equilibrium contact angle θ. The radius r of the circumference at the solid liquid interface can be written as[32]

$$r = \left(\frac{4}{\beta}\right)^{1/3} R\sin\theta, \qquad \beta = (1 - \cos\theta)^2(2 + \cos\theta) \tag{6}$$

Where R is the radius of the drop prior deposition. The net adhesive force F_a acting along x may be therefore estimated,[33,34] being

$$F_a = \int_{-\pi/2}^{\pi/2} \gamma_{lv}(\cos\theta_r - \cos\theta_a) r\cos\varphi\, d\varphi = 2r\gamma_{lv}(\cos\theta_r - \cos\theta_a) \tag{7}$$

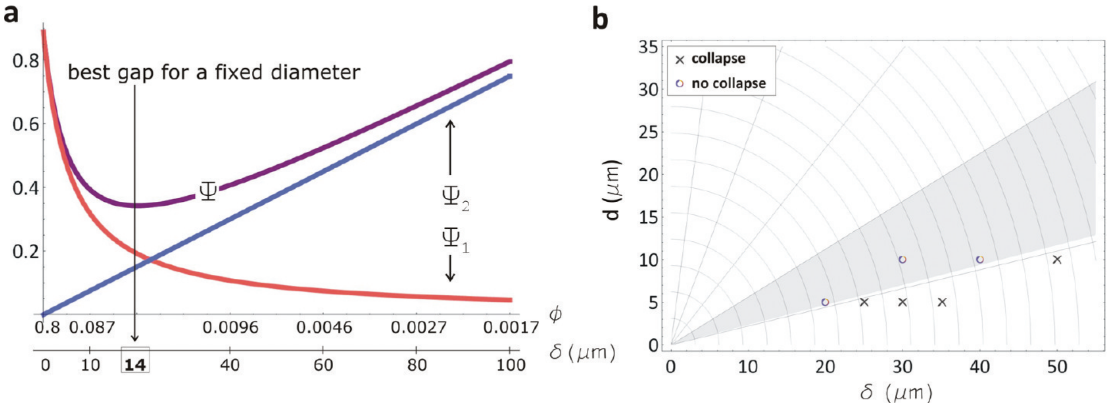

Figure 3. A superhydrophobic surface can be patterned as to reproduce a regular lattice described by the diameter d of the pillars and the gap δ between those pillars. The nondimensional function Ψ depends on d and δ not separately. For a fixed d, the gap where the value of Ψ takes a minimum is the gap of optimal design that guarantees the best performance of the substrate (a). The stability region, in light gray in the diagram, recovers all the combinations of optimal design, and this is confirmed by a number of different experiments (b).

where the advancing (θ_a) and receding (θ_r) angles are the front and rear angle in direction of droplet motion (see also the Supporting Information #1), and thus, the adhesion force F_a would depend upon the width of the contact line (2r), the liquid−vapor surface tension (γ_{lv}), and the term ($\cos\theta_r - \cos\theta_a$) that is proportional to the contact angle hysteresis CAH, $\theta_a - \theta_r$. Assume now to deposit the same drop upon a microtextured, artificial surface. In revisiting eq 7, it should be considered that (i) the radius r of the solid liquid contact is reduced due to the increased contact angle and (ii) the CAH the drop *senses* is not unique in view of the composite, heterogeneous surface it is placed upon (the CAH is maximum at the solid fraction, zero otherwise). Relation 7 can be thus rewritten as

$$F_a^c = 2r^c\langle\gamma_{lv}(\cos\theta_r - \cos\theta_a)\rangle = 2r^c\gamma_{lv}(\cos\theta_r - \cos\theta_a)\phi \tag{8}$$

where <|> is the spatial average taken on the surface of contact of the drop, and it is here assumed that the radius of contact is large compared to the pillars' dimension. From this, it follows that tiling the surface increases hydrophobicity and dramatically reduces adhesion. Eq 8 can be expanded to read

$$F_a^c = 4^{5/6}R\gamma_{lv}\frac{\sqrt{1-(\phi(\cos\theta+1)-1)^2}}{((1+\phi\cos(1+\theta))(2-\phi\cos(1+\theta))^2)^{1/3}}(\cos\theta_r - \cos\theta_a)\phi \tag{9}$$

The ratio $\zeta = F_a^c(\phi = 1)/F_a^c(\phi)$ gives a measure of the increased ability of a drop to slip or slide over SHSs (Figure 2d). ζ is a function of ϕ, and the lower ϕ, the less friction matters. A solid fraction of one percent ($\phi = 0.01$) would induce adhesion forces that are some 10^3 times less important than for a continuous surface. Also notice that ζ decreases with the initial contact angle θ, while it is practically constant for sufficiently large values of θ. Consider now a droplet positioned upon a SHS. The solvent evaporates over time, and thus, the volume of the drop decreases. On account of this, also the contact angle decreases. This fact unbalances the forces acting upon the drop and would generate a radial pressure that tends to recall the contact line toward the center of the drop, thus recovering the initial equilibrium contact angle θ_c (Figure 2e). The total force along x that is generated is

$$F_p = 2r^c\gamma_{lv}(\cos\theta_{ne} - \cos\theta_c) \tag{10}$$

where θ_{ne} is the nonequilibrium contact angle as in Figure 2e; the condition for depinning is thus $F_p > F_a^c$. If $F_p \leq F_a^c$, the drop is stuck on the surface. (This condition may be valid, strictly speaking, in close proximity of θ_c.) The ratio $\mathbf{Y} = F_p/F_a^c$ is an index the propensity of a drop to slide upon a surface. When $\mathbf{Y} > 1$, depinning dominate over friction, and thus, the drop is recalled toward its center during evaporation. In Figure 2f, $\mathbf{Y}$ is plotted against θ_{ne} at different ϕ's. At the initial time, $\mathbf{Y} < 1$, and this means that the drop is sticky. As the evaporation process continues, θ_{ne} decreases. The depinning force augments with time and so does $\mathbf{Y}$. When $\mathbf{Y}$ is sufficiently large, that is $\mathbf{Y} \gg 1$, the contact line of the drop would recede, and the contact angle would again coincide with the expected equilibrium contact angle θ_c. Under these conditions, $\mathbf{Y} = 0$. The process would then start over again with the repetition of the same mechanism. Notice that the drop would experience a different story line on changing ϕ. When ϕ is small, $\mathbf{Y}$ varies more rapidly with θ_{ne}, and the condition for radius downturn is met at earlier stages of evaporation. In any case, at each cycle, the contact radius is reduced by a quantity that is the distance between two lines of pillars. When r goes down below the critical radius of impalement, an irreversible transition to Wenzel occurs, whereby the drop is stuck. For sufficiently high pillars, the minimum contact radius achievable (and thus, the final theoretical size of the drop upon evaporation) is limited by energetic considerations, being[35−37]

$$r_{min} \propto \frac{\delta}{\cos\theta} \tag{11}$$

where δ is the gap between two spots. Noticeably, the final size of the drop does not depend upon its original size but rather by a mixture of the geometrical (that is, the gap) and chemical (that is, contact angle measured upon the flat, nonstructured surface) parameters of the substrate.

2.4. Considerations for an Optimal Design.

The models above predict that the contact angle is large, and thus, the contact area is limited, provided that the pillars are sparse or, equivalently, that ϕ is small (eq 2). Unfortunately, the collateral effect of small ϕ is that a drop would collapse at the early stage of the evaporation process (eq 11). In this case, the drop would stick on the surface and the solute would redistribute as to form a ringlike structure along the water−solid line of contact, with no or minor concentration effects. The coffee ring effect is very well understood and it is attributed to a fixed contact line and to an outward flow within the drop.[38,39] Here, a criterion is discussed that would guarantee the best trade-off between sufficiently dense forests of pillars, that prevent the early collapse of the drop and avoid the dispersion, and sparse structures, that instead ensure large contact angle.

Let the surface be patterned as to reproduce a regular lattice described by the diameter d of the pillars and the gap δ between those pillars. Notice that the gap δ is different from the pitch p, and these two variables, and the diameter d, are linked by relation $p = d + \delta$. If d is fixed, then the system would be determined given the sole δ. The aim here is to determine the optimal δ^0 that would induce large θ_c still retaining the advantages of a small r_{min}. To do this, we introduce the function Ψ as the sum of the two nondimensional contributions Ψ_1 and Ψ_2, $\Psi = \Psi_1 + \Psi_2$.

Ψ_1 accounts for the effects of the microstructure on the contact line. It is derived from the radius of contact r as in eq 4, being $\Psi_1 = r/R$. Ψ_1 depends upon θ_c and thus, through eq 2, ϕ. The smaller ϕ, the is smaller Ψ_1 (Figure 3a).

Ψ_2 instead accounts for the effects of the microstructure upon the smallest radius of contact prior to the drop collapse. It is derived by the minimum contact radius r_{min} as in eq 9, being

$$\Psi_2 = \frac{r_{\mathrm{min}}}{d} = \frac{\delta}{d\cos\theta} = \frac{1}{\cos\theta}\frac{1-\sqrt{\phi}}{\sqrt{\phi}} \qquad (12)$$

Differently from Ψ_1, Ψ_2 is inversely proportional to ϕ (Figure 3a). While Ψ_1 and Ψ_2 are monotonic, their sum is not. A value of ϕ, and accordingly δ, exists where Ψ attains a minimum (Figure 3a), and this would be the best gap for a fixed d. The optimal values of δ were calculated for d ranging from 0 to 30 μm. This region of best design is represented in the diagram of Figure 3b. In the same diagram, a number of points is also reported. These represent evaporation experiments, where an excess of Rhodamine in D.I. water (concentration 10^{-4} M) was used to verify the concentration capabilities of different patterns (Supporting Information #3). When the pillars are sufficiently dense, the drop successfully slips upon the posts and the solute gets concentrated, in accordance with the model. When the pillars are sparse, collapse occurs. This is a remarkable result in that the concentration process of a solute over a micropatterned substrate can be predicted and controlled with good accuracy. In general, d should be as small to consent to a sufficiently large number of pillars to interact with the drop.

3. MATERIALS AND METHODS

Rhodamine R6G, myoglobin, ribonuclease B, lysozyme, and sodium chloride were purchased from Sigma. Deionized (D.I.) water (Milli-Q Direct 3, Millipore) was used for all experiments. All chemicals, unless mentioned otherwise, were of analytical grade and were used as received. Rhodamine6G is an organic compound and is used extensively in biotechnology applications. It is a dye which can be observed very clearly by fluorescence microscopy. Its absorption and emission wavelength are 530 and 556 nm, respectively.

Small drops ($V < 10$ μL, $R < 1.35$ mm) of D.I. water containing infinitesimal amounts of analytes were gently posted upon the surfaces, and the entire process of evaporation was followed over time. An automatic contact angle meter (KSV CAM 101, KSV INSTRUMENTS LTD, Helsinki, Finland) was used at room temperature. Please notice that the energy of adhesion γ per unit area at the gas/water interface is ~72.8 mJ/m^2 at 20 °C. The process enabled one to concentrate very tiny amounts of agents over micrometric areas. The evaporation processes were performed in a clean room to reduce the presence of external contaminants and lasted approximately 30 min. The residual solute was observed using scanning electron microscopy (SEM), fluorescent microscopy, and Raman spectroscopy techniques.

3.1. Fabrication of the Devices. Artificial superhydrophobic surfaces were fabricated. These are textures comprising a periodic hexagonal lattice of cylindrical Si micropillars with a certain diameter and pitch. Nanosized geometries appropriately positioned upon the pillars would ensure giant SERS enhancement. (100) silicon wafers (from Jocam, Milan, Italy) were cleaned with acetone and isopropanol to remove possible contaminant and then etched with a 4% wet HF solution. The wafers were then rinsed with DI water and dried with N_2. Standard optical lithography techniques (Karl Suss Mask Aligner MA 45, Suss MicroTec GA, Garching, Germany) were employed to dig regular arrays of disks within a layer of positive resist (S1813, from Rohm and Haas) that was spin-coated onto clean silicon wafers. Electroless deposition techniques were employed to grow silver nanograins within the holes. Upon removal of the residual resist with acetone, a Bosch Reactive Ion Etching (MESC Multiplex ICP, STS, Imperial Park, Newport, UK) process was utilized whereby the final structures were obtained in the form of cylindrical pillars with an aspect ratio greater than 2. The electroless grown Ag layer served as mask during the reactive ion etching (RIE) process, while its characteristic granular structure allowed for the enhancement of the SERS signal. The substrates, as a whole, were then covered with a thin (few nm) film of a Teflon-like (C_4F_8) polymer to ensure hydrophobicity; to do this, a modified Bosch/RIE process was utilized, where solely the passivation mode was activated. In this phase, all gas flows, including SF6, Argon, and Oxygen, are set to zero, with the exception of the chemical inert passivation layer C4F8. The masks necessary for optical lithography were fabricated using standard electron beam lithography (Crestec CABL-9000C electron beam lithography system) methods. The cartoon in the Supporting Information #4 recapitulates the fabrication process.

The electroless deposition on a substrate is based on an autocatalytic or a chemical reduction of aqueous metal ions. This process consists of an electron exchange between metal ions and a reducing agent. In this work, Si substrate was used itself as reducing agent. A fluoridric acid (HF) solution containing silver nitrate ($AgNO_3$) was used, where Ag was reduced to metal form by the Si substrate oxidation. In particular, the patterned silicon wafer was dipped in a 0.15 M HF solution containing 1 mM silver nitrate for 60 s at a constant temperature $T = 313$ K. After the growth process, the silicon wafer was rinsed with water and dried under nitrogen flux. The driving force in this process is the difference between redox potentials of the two half-reactions, which depends on solution temperature, concentration, and pH. Consequently, these parameters influence the particles size and density.

3.2. Samples SEM Characterization. SEM images of the samples were captured using a Dual Beam (SEM-FIB)-FEI Nova 600 NanoLab system. During the acquisitions, beam energies of 5 and 15 keV, and corresponding electron currents of 0.98 pA and 0.14 nA, were used. In some cases, the mode 2 configuration was used, whereby images can be magnified over 2500 k× and ultrahigh resolution may be achieved. In this modality, the immersion lens was switched on and the TLD detector in Secondary Electron operation was used.

3.3. Sample Atomic Force Microscopy Characterization. Atomic force microscopy (AFM, Veeco MultiMode with NanoScope V controller) was used for the measurements of the silver nanograin assemblies. The measurements were performed in a dry environment in intermittent contact mode over a sampling area of 6000 × 6000 nm^2. Room temperature was fixed for all the acquisitions. Ultrasharp Si probes (ACLA-SS, AppNano) with a nominal tip radius less than 5 nm were used for high resolution. Multiple measurements were done in different scan directions to prove the avoidance of artifacts. The images had a resolution of 1024 × 1024 points and were acquired at a scanning rate of 1 Hz. The images obtained were processed with the WSxM software, using either flattening or plane fit according to the relief characteristics, with the minimal polynomial order needed. Using conventional mathematical procedures implemented in Mathematica, the roughness and fractal dimension of the samples were derived.

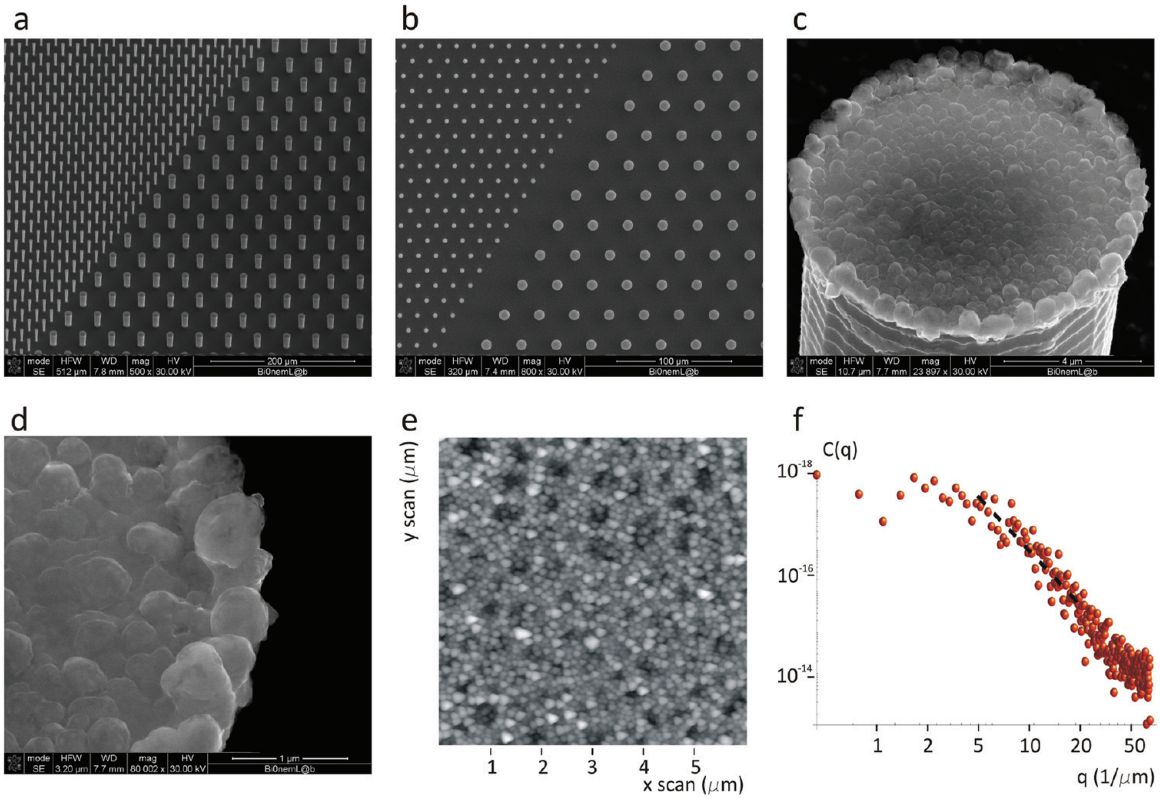

Figure 4. SEM images of the micropillars of which the superhydrophobic surface is composed; the pillars are arrayed to form regular geometries and these cover regions as large as several hundreds of micrometers without defects or imperfections (a,b). Larger magnifications reveal, at smaller scales, silver nanoparticles aggregates (c,d). AFM image (e) and characteristic power spectrum (f) of the silver nanoparticles aggregates.

3.4. Fluorescence Microscopy Characterization of Rhodamine Deposits.

Fluorescence microscopy measurements were performed using an inverted microscope, with infinity-corrected optics (Nikon-ECLIPSE TE 2000-U). The microscope objectives used were a Plan Fluor 40x and a Plan Apo 60x, with 0.75 and 0.95 numerical apertures. For probe excitation, a violet diode laser source emitting at 408 nm, an argon source emitting at 488 nm, and Helium Neon laser source emitting at 543 nm were used. A Nikon D-Eclipse C1 scanning head with three channels was utilized for the measurements.

3.5. Raman Characterization of Rhodamine Deposits.

Microprobed Raman spectra were obtained using Renishaw inVia Raman microscope at room temperature through a 20× objective of a Leica microscope. The Raman spectra were excited by the 514.0 nm line of an Ar^+ laser in backscattering geometry. The laser power was 0.18 mW with an integration time of 20 s. Mapping Raman measurements were carried out with the step size 19.50 and 34.60 μm in the *x*- and *y*-axis directions, respectively.

4. RESULTS

Several SEM micrographs of the SHSs were taken over different samples to assess uniformity and reproducibility. In Figure 4a,b, silicon pillars are arrayed over large square areas sizing up to some millimeters per side, with no or minor defects in the structures which thus recover a perfect hexagonal lattice. This would verify the fabrication process capability to attain extreme control over the key characteristics of the micropillars such as shape and size, at least on a large scale. On a smaller scale, as in Figure 4c,d, the head of the pillars is covered by silver nanograin clusters. The AFM image of Figure 4e shows that the grains are randomly distributed with an average grain size of about 50 nm and a small standard deviation Sd = 20 nm. From this, using custom-made algorithms, a power spectrum was deconvoluted and the average roughness Ra and the fractal dimension Df were consequently derived, being Ra ∼ 34 nm and Df ∼ 2.34. Notice that the average grain size and roughness are consistent with a local enhancement of the Raman signal in the order of 10^6.[40] Interestingly, while the influence of surface profile, and especially roughness, upon the Raman signal has been reported in a number of different works, only a few have been focusing on the effect of more sophisticated parameters such fractal dimension, that instead deserves to be investigated even further.

The detection capabilities of these devices were verified using, as a probe, Rhodamine6G (R6G); few molecules of R6G were conveniently analyzed as described below. R6G has some biological interest in that it is an organic compound used extensively in biotechnology applications. Most importantly, R6G is very well-known and characterized, and thus, any result involving R6G can be unequivocally interpreted and used as a basis for reliable conclusions and for planning further analysis or strategies.

Solutions were prepared containing R6G molecules with a concentration as low as 10^{-18} M. Evaporation processes of small drops of solution were followed over time until an irreversible transition to a pinning state occurred. Few molecules were conveniently enforced to confine into a small area, at the limit upon a single pillar. The extremely small final size of the deposit depends on the reduced friction of the device, and this is evidenced in the Supporting Information #5, where the dynamics of evaporation, and especially the contact angle and contact area of the drop over time, are followed for either a continuous, nominally flat surface or a microstructured, superhydrophobic surface. Differently from the nonstructured surface, the SHS exhibits a contact angle that is pretty stable

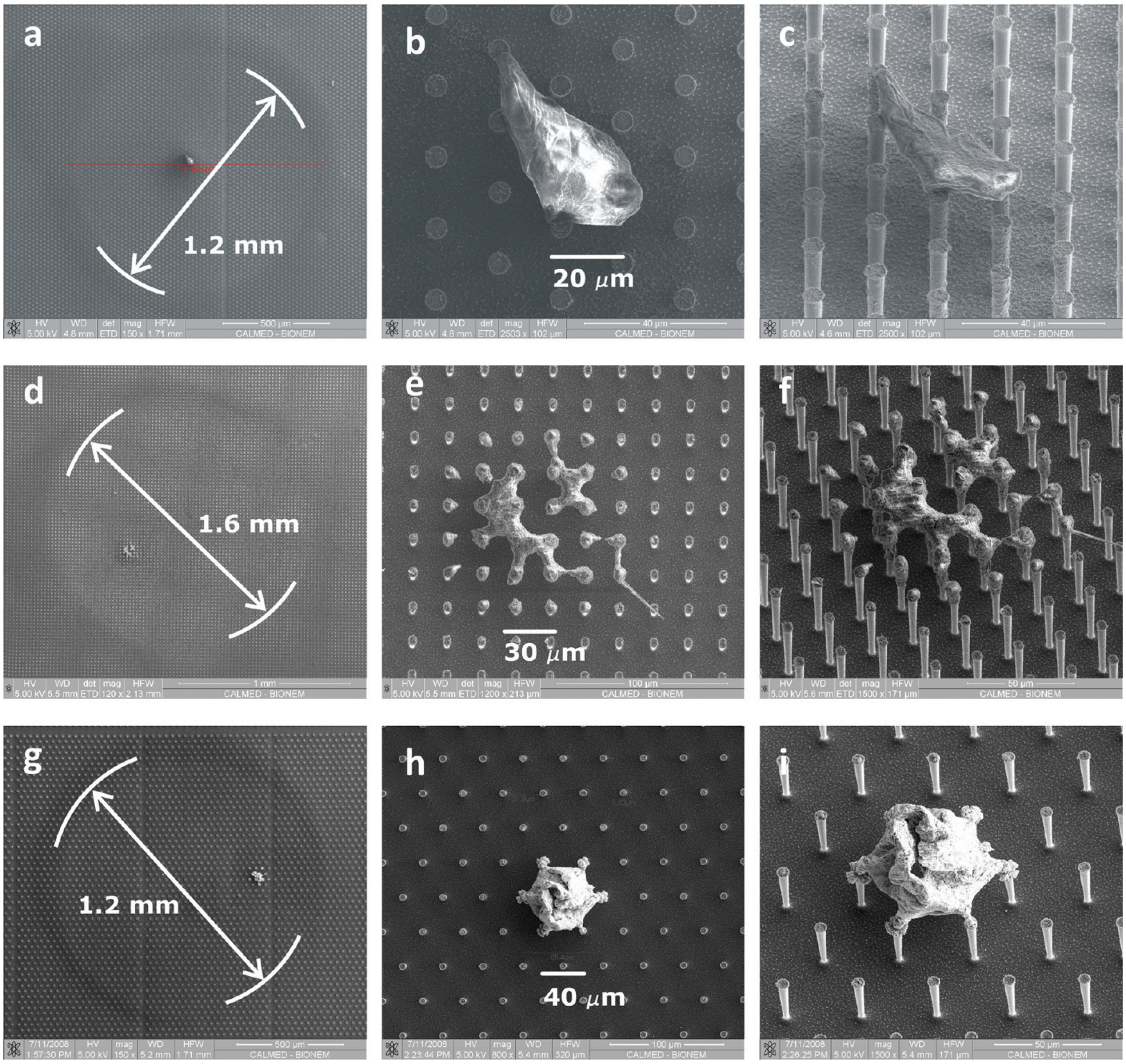

Figure 5. SEM micrographs of the residual solute of R6G upon evaporation on a superhydrophobic surface, at magnifications ranging from 150× to 2500×. The initial footprint of the drop measures up to about 1.6 mm (d) and on average 1.2 mm (a,g), while the solution, at the final stage of the process, sediments in a bounded region sizing few tens of micrometers or less (b,e,h). The tilted images demonstrate that the solute is accumulated entirely upon the pillars, without touching the bottom of the substrate (c,f,i).

over time, and this would demonstrate that the evaporation, in this case, is a self-similar process: the drop undergoes a scale transformation whereby the volume is reduced while the shape remains constant in time. More interestingly, in the case of the SHS, the contact area decreases down to roughly one tenth (10%) of the initial deposition surface, while the friction coefficient is definitely more important for the continuous surface, where the final contact area is, at most, 0.6 times the initial (Figure S8d, Supporting Information).

Figure 5 shows a collection of SEM images of the residual solute of R6G at different magnifications ranging from 150× to 2500×. The initial footprint of the drop measures up to about 1.6 mm (Figure 5d) and, on average, 1.2 mm (Figure 5a,g), while the solution, at the final stage of the process, sediments in a bounded region sizing few tens of micrometers or less. Considering bidimensional scale effects solely, the device is capable of concentrating a solution some $(1200/40)^2-10^3$ times. More importantly, all the deposits are suspended upon the pillars (Figure 5c,f,i). The residual R6G is arranged in complex forms or agglomerates that wrap the pillars, connecting them one to the other, without touching the bottom of the substrate.

Upon evaporation, the analyte would thus be distributed over a small area that typically includes more than one pillar. The analyte is roughly homogeneous over this area. Notice that the analyte deposition profile is uniform, rather than ring-shaped, on account of the reduced friction of SHSs, whereby Marangoni effects can be neglected. Nevertheless, the exact solution of the problem of the mass transfer and distribution in a single evaporation droplet is very complex and is governed by the concentration gradient of chemical species and by the convection−diffusion (advection) equations for species and product. Moreover, the initial and boundary conditions to the problem, including the initial concentration of the species, the temperature, and humidity of the system, or the presence of impurities or defects on the surface, play a major role. In other terms, the exact, final shape of the solute is basically unpredictable, and this is why the shapes in Figure 5b,e,h are

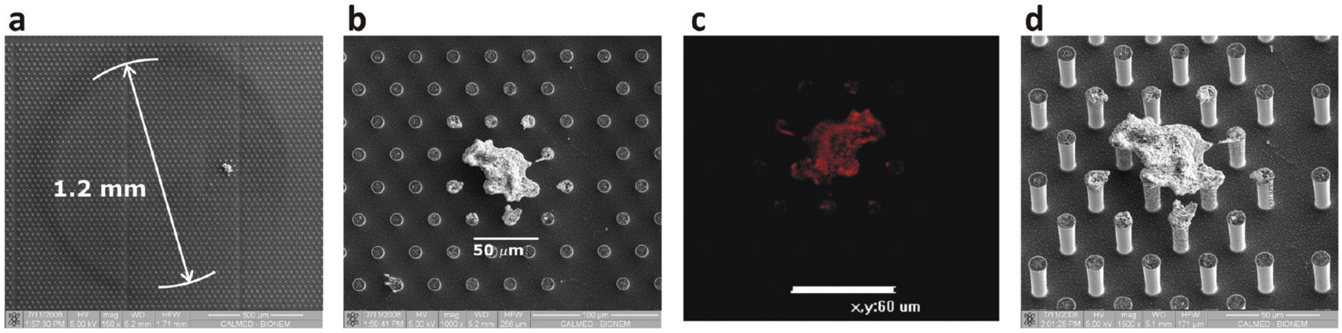

Figure 6. SEM micrographs of the residual solute of R6G upon evaporation on a superhydrophobic surface at low (a) and high (b) magnification. Confocal fluorescence image of the same deposit (c). Tilted SEM image of the sample (d).

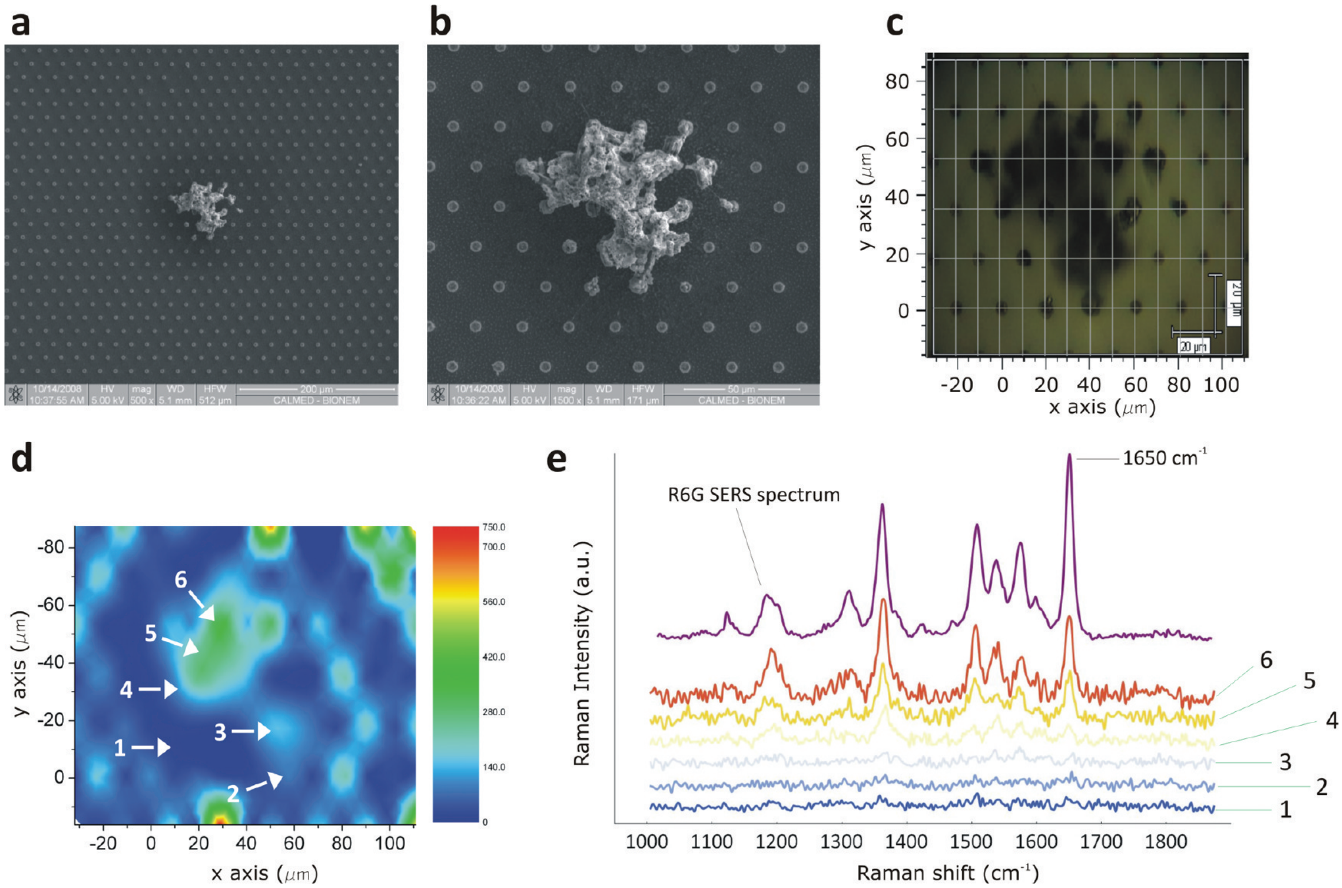

Figure 7. SEM (a,b) and Raman (c,d) measurements for a Rhodamine deposit originated from a drop with an initial concentration of 10^{-18} M. The 2D intensity Raman map of Rhodamine as in (d) is derived from a series of single SERS spectra, acquired in different positions of the substrate, some of which are presented in (e). The spectra are pretty similar in shape, that is, the principal peaks are preserved moving from a point to another, and this would guarantee that SERS measurements are repeatable. The spectra are instead different in intensity, and this scale effect means that the device senses, point by point, a variable Raman signal, that is roughly proportional to the quantity of Rhodamine on the substrate.

different. Despite this, a correct design of the surface would always induce small and very well recognizable, biological residues upon evaporation. Notice, incidentally, that the Rhodamine deposit in Figure 5h is hexagonal, and this is obviously correlated to the fundamental motif of the pillars.

Fluorescent images in Figure 6 would prove that identification of the residue as R6G is correct, and it is not instead constituted by debris or other refuses. The intensity of fluorescence is directly proportional to the quantity of substance deposited upon the pillars, and thus, in the central part of the substrate, the amount of R6G is higher and it diminishes as we move toward the sides. Notice how the intensity of the signal of fluorescence in Figure 6c reproduces faithfully the solute profile over the substrate as in the SEM micrographs in Figure 6a,b,d.

Micro-Raman mapping measurements were performed to further substantiate the method. Figure 7 shows SEM (Figure 7a,b) and Raman (Figure 7c,d) measurements for a Rhodamine deposit originated from a drop with an initial concentration of 10^{-18} M. Figure 7e shows the SERS spectra, acquired in different positions of the substrate, compared to a reference Raman spectrum of R6G, used as a control. All the spectra are pretty similar in shape, that is, the principal peaks are preserved moving from a point to another, and this would guarantee that

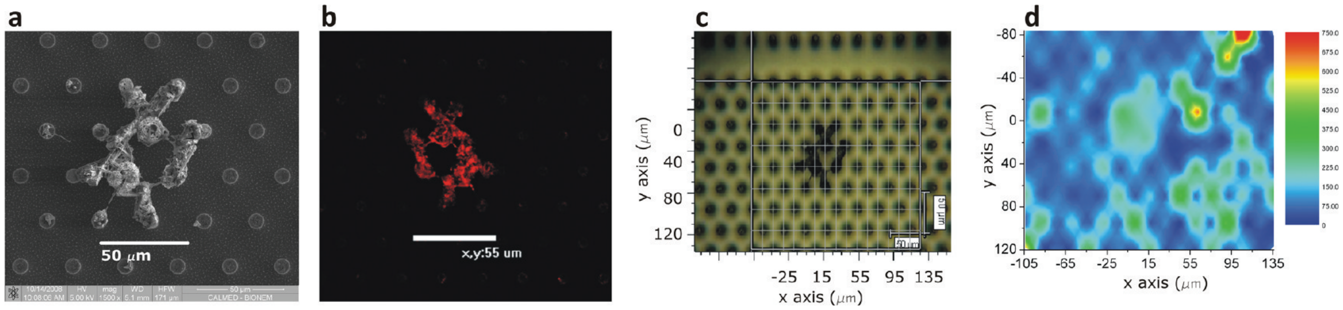

Figure 8. SEM image (a), confocal fluorescence image (b), and Raman mapping measurement (c, d) of a Rhodamine deposit upon evaporation. Initial concentration = 10^{-18} M.

SERS measurements are repeatable. The spectra are instead different in intensity, and this scale effect means that the device senses, point by point, a variable Raman signal, that is roughly proportional to the quantity of Rhodamine on the substrate. Using the band centered at 1650 cm^{-1} as a reference,[20] the single spectra were used to derive a 2D intensity Raman map of Rhodamine, as reported in Figure 7d.

The residue of another evaporation process of Rhodamine, with initial concentration = 10^{-18} M, is examined in Figure 8. R6G molecules are revealed using SEM (Figure 8a), confocal fluorescence (Figure 8b), and SERS (Figure 8c,d) imaging techniques. While conventional Raman intensity is directly proportional to the number of molecules probed, in the case of SERS, if the molecules are not in close proximity of the nanometallic substrate ensuring the enhancement of the electric field, the resulting spectral amplitude would dramatically drop off, and thus, the thicker the layer of Rhodamine, paradoxically the lower is the signal. This would explain why the intensity signals in some regions of the diagrams in Figure 8d are not consistent with SEM or fluorescence images. In the Supporting Information #6, the single SERS spectra, which were used to reconstruct the mapping profile in Figure 8d, are reported.

5. DISCUSSION

Treatment of cancer patients is greatly facilitated by detection of the cancer prior to metastasis. Nevertheless, the effective early detection of precancerous and neoplastic lesions remains an elusive goal. Advanced clinical cancer imaging technologies, including MRI (magnetic resonance imaging), PET (positron emission tomography), C-T (computerized tomography) scans, or medical ultrasonography, do not possess sufficient spatial resolution for early detection based on lesion anatomy. Moreover, these imaging technologies most often require advanced and exclusive machines whereby they are very expensive and would not, therefore, be affordable and easily accessible to a large portion of the population.

An effective evaluation of pathologies can be instead addressed based on molecular expression profiles. It is very well understood that blood contains a treasure trove of biomarkers that could reflect the ongoing pathological state of tissues or organs. Every cell in the body leaves a record of its physiological state in the products it sheds to the blood, either as waste or as signals to neighboring cells. This hidden signature of diseases waits just to be decoded and revealed. In sight of this understanding, microbiologic, immunologic, and molecular analysis of tissue and cells are becoming indispensable clinical platforms for rendering pathologic evaluation. Collectively, these diagnostic modalities are critical for determining the appropriate medical treatment. Conventional immunoassay methods, including enzyme-linked immunosorbent assay (ELISA), fluorescence immunoassay, magnetic bead based electrochemilumincence (ECL), chemiluminescence, liquid chromatograpy-mass spectrometry (LC-MS), and immuno-polymerase chain reaction (PCR) assay, allow reliable protein detection.

However, these approaches, all in all, lack the requirements for point-of-care diagnosis which require the sensor to be rapid, operationally simple, low cost, and highly sensitive to address both levels of the biomarkers in normal and cancer patient serum. Sensitivity, in particular, is the main concern for these methods, in that very often the peptides of interest are severely diluted at the early stages of diseases and are therefore practically *invisible* for the majority of these technologies. For all this, blood serum is not yet used as a routine screening procedure.

To date, and rather surprisingly, surgical biopsy remains the *gold standard* for the clinical assessment of the pathologic basis of disease. The morphologic presentation of tissue specimens continues to be the backbone of diagnostic pathology, with the clear disadvantage that the quality of diagnoses is entrusted with the pathologist's experience, and thus, this practice inherently suffers from being predominately a qualitative art.

In the past decades, original strategies, technologies, or both were developed to defeat the limitations of clinical imaging technologies, conventional immunoassay methods, and biopsies. These strategies are complementary, in the sense that one may be used in conjunction with the others, and include the use of mass spectrometry or Raman or other spectroscopies for the analysis of molecules, biomolecules, or individual peptides; nanoscale devices for the enhancement of the light/matter interaction and the applications thereof, such as SERS substrates; superhydrophobicity for the manipulation of biological solutions.

Individually, the technologies above are surely important. When combined, these elements allow one to create unique devices where unprecedented properties emerge and may be used to afford otherwise untreatable medical problems. The major advance, here, is that at least three different technologies are conveyed into a single platform.

Biology does a lot with a little. Learning from nature, and inspired by the lotus effect, we developed a new nanotechnology that, mimicking the morphology of the lotus leaf, offers realistic possibilities to diagnosis tumors at their early stage. Our biodevices are hybrid systems that incorporate hierarchically features at the micro- and nanoscales. On account of their multiscale nature, they permit one to transport target molecules in extremely dilute solutions to nanoplasmonic sensors, surpassing the impractical time scales that these devices typically suffer from. In tests with Rhodamine molecules, we found that these devices provide concentration factors of several orders of magnitude over a conventional, flat plasmonic substrate, and in fact, we could detect molecules in the dramatically low concentration range of 10^{-18} M.

Indeed, the concept of using SHSs for analyzing biological solutions is not completely new. In a recent work, Xu F. et al.[41] demonstrated that zinc oxide nanorods, conveniently covered with silver nanoparticles, are superhydrophobic, and this increased hydrophobicity allows important condensation of the solute and an improved SERS signal thereof, that can be as large as three times the signal acquired on a conventional Ag/ZnO substrate. Nevertheless, our work significantly differs from the other described method. Here, we introduced a two scale system, where the diameter of the micropillars and the size of the silver nanograins can be controlled independently. We also introduced mathematical models to describe the effects of these parameters on the wettability of the substrate, the stability of the drop, the enhancement of surface-adsorbed molecule signature. In other terms, we provided new instruments for the rational design of SHSs, which can be conveniently engineered according to the problem at study. Most importantly, the SERS signal improvement that we reported cannot be ascribed to concentration effects solely. More relevant than concentrating a solution, these devices are capable to manipulate, move, and vehicle molecules with a good precision to certain regions of the substrate: our scheme provides the capability of localization and immobilization of molecules where the electric is more intense. To this extent, our devices are smart biological platforms.

The single detection issue is a worthwhile aim in itself; nevertheless, the introduction of superhydrophobicity in life sciences opens up a number of different applications and opportunities. Microdrops provide environmental characteristics which are difficult to obtain otherwise. Using these conditions to investigate life processes affords opportunities for discovery and development of applications which enhance research and the probability for pathfinding mechanisms in life processes. The physics of drops, where gravity has minor effects, and interfacial forces dominate over volume, affords a new window through which to observe life processes. It is a probe which can reveal novel mechanisms that are fundamental to cell processes, disease process, and the adaptation of living systems to changes in physical forces.

Moreover, SHSs provide an opportunity to better understand interfacial phenomena, such as the wetting and spreading of immiscible liquids or the spreading of fluid across a solid surface. Given the sizes of interest, which are small, wetting determines the configuration and location of fluid interfaces, thus greatly influencing, if not dominating, the behavior of multiphase fluid systems. Phenomena, processes, and procedures that may be investigated in this context include cell culture, formation and stability of nanoemulsions, transportation phenomena, self-organization phenomena, advancement of analytical devices, protein crystal growth, formation, and organization.

6. CONCLUSIONS

In this work, a new family of devices is described where the micro- and nanoscales combine and activate new functions which can boost the detection of a few molecules. Silicon substrates were conveniently patterned to include regular hexagonal lattices of micropillars, while the top of the pillars was further modified to incorporate silver nanograins clusters. Those substrate are superhydrophobic because of the architecture at the microscale, while they reveal superior SERS capabilities on account of the nanoscopic size of the metal particles clusters. The devices were designed and fabricated using convenient mathematical models and advanced nanotechnologies. Thereafter, direct experiments with solutions of Rhodamine with initial concentration 10^{-18} M proved their capability of (i) condensing otherwise poorly concentrated solutions, (ii) transporting the analytes of interest to the active sites of substrate with high precision and reduced times, and (iii) detecting and recognizing molecules in fairly low abundance ranges. This novel procedure, at the forefront of SERS and superhydrophobicity, was conceived and developed in sight of the intrinsic limitations of conventional biophotonic devices. The correct integration of this technology with assessed biological and proteomic methods could represent the way to resolve the early cancer detection issue.

■ ASSOCIATED CONTENT

Ⓢ Supporting Information

Additional data on the characterization of the PSi substrates and on cell adhesion and complementary information to the Materials and Methods section. This information is available free of charge via the Internet at http://pubs.acs.org/.

■ AUTHOR INFORMATION

Corresponding Author

*E-mail: gentile@unicz.it. Phone:+39 0961 369 5896.

Notes

The authors declare no competing financial interest.

■ ACKNOWLEDGMENTS

This work was funded under European Project SMD FP7-NMP 2800-SMALL-2 (proposal no. CP-FP 229375-2), Italian project FIRB "Rete Nazionale di Ricerca sulle Nanoscienze ItalNanoNet" (cod. RBPR05JH2P-010) and the EU Commission, the European Social Fund and the Calabria Region (POR Calabria FSE 2007-2013).

■ REFERENCES

(1) Theis, T.; Parr, D.; Binks, P.; Ying, J.; Drexler, K. E.; Schepers, E.; Mullis, K.; Bai, C.; Boland, J. J.; Langer, R.; Dobson, P.; Rao, C. N. R.; Ferrari, M. *Nat. Nanotechnol.* **2006**, *1*, 8−10.

(2) Whitesides, G. M. *Nat. Biotechnol.* **2003**, *21* (10), 1161−1165.

(3) Gentile, F.; Tirinato, L.; Battista, E.; Causa, F.; Liberale, C.; Di Fabrizio, E; Decuzzi, P. *Biomaterials* **2010**, *31* (28), 7205−7212.

(4) Gentile, F.; La Rocca, R.; Marinaro, G.; Nicastri, A.; Toma, A.; Paonessa, F.; Cojoc, C.; Liberale, C.; Benfenati, F.; Di Fabrizio, E.; Decuzzi, P. *ACS Appl. Mater. Interfaces* **2012**, DOI: 10.1021/am300519a.

(5) Perennes, F.; Marmiroli, B.; Matteucci, M.; Tormen, M.; Vaccari, L.; Di Fabrizio, E. *J. Micromech. Microeng.* **2006**, *16* (3), 473−479.

(6) Perozziello, G.; La Rocca, R.; Anichini, A.; Cojoc, G.; Liberale, C.; Malara, N.; Candeloro, P.; Tirinato, L.; Gentile, F.; Coluccio, M. L.; Carbone, E.; Di Fabrizio, E. *Small* **2012**, DOI: 10.1002/smll.201200160.

(7) Calimeri, T.; Battista, E.; Conforti, F.; Neri, P.; Di Martino, M. T.; Rossi, M.; Foresta, U.; Piro, E.; Ferrara, F.; Amorosi, A.; Bahlis, N.; Anderson, K. C.; Munshi, N.; Tagliaferri, P.; Causa, F.; Tassone, P. *Leukemia* **2011**, *25*, 707−711.

(8) Tasciotti, E.; Liu, X.; Bhavane, R.; Plant, K.; Leonard, A. D.; Price, B. K.; Ming-Cheng Cheng, M.; Decuzzi, P.; Tour, J. M.; Robertson, F.; Ferrari, M. *Nat. Nanotechnol.* **2008**, *3* (3), 151−157.

(9) De Angelis, F.; Pujia, A.; Falcone, C.; Iaccino, E.; Palmieri, C.; Liberale, C.; Mecarini, F.; Candeloro, P.; Luberto, L.; de Laurentiis, A.; Das, G.; Scala, G.; Di Fabrizio, E. *Nanoscale* **2010**, *2*, 2230−2236.

(10) Ferrari, M. *Nat. Rev. Cancer* **2005**, *5*, 161−171.

(11) Gaspari, M.; Ming-Cheng Cheng, M.; Terracciano, R.; Liu, X.; Nijdam, A. J.; Vaccari, L.; Di Fabrizio, E.; Petricoin, E. F.; Liotta, L. A.; Cuda, G.; Venuta, S.; Ferrari, M. J. *Proteome Res.* **2006**, *5*, 1261−1266.

(12) Liotta, L. A.; Ferrari, M.; Petricoin, E. F. *Nature* **2003**, *425*, 905−905.

(13) Posasadas, E. M. *Ann. Oncol.* **2005**, *6*, 16−22.

(14) Das, G.; Mecarini, F.; Gentile, F.; De Angelis, F.; Kumar, M.; Candeloro, P.; Liberale, C.; Cuda, G.; Di Fabrizio, E. *Biosens. Bioelectron.* **2009**, *24*, 1693−1699.

(15) Kneipp, K. *Phys. Today* **2007**, *60* (11), 40−47.

(16) De Angelis, F.; Patrini, M.; Das, G.; Maksymov, I.; Galli, M.; Businaro, L.; Andreani, L. C.; Di Fabrizio, E. *Nano Lett.* **2008**, *8* (8), 2321−2327.

(17) De Angelis, F.; Das, G.; Candeloro, P.; Patrini, M.; Galli, M.; Bek, A.; Lazzarino, M.; Maksymov, I.; Liberale, C.; Andreani, L. C.; Di Fabrizio, E. *Nat. Nanotechnol.* **2010**, *5*, 67−72.

(18) De Angelis, F.; Liberale, C.; Coluccio, M. L.; Cojoc, G.; Di Fabrizio, E. *Nanoscale* **2011**, *3*, 2689−2696.

(19) Weitz, D. A.; Gramila, T. J.; Genack, A. Z.; Gersten, J. I. *Phys. Rev. Lett.* **1980**, *45* (5), 355−358.

(20) Coluccio, M. L.; Das, G.; Mecarini, F.; Gentile, F.; Pujia, A.; Bava, L.; Tallerico, R.; Candeloro, P.; Liberale, C.; De Angelis, F.; Di Fabrizio, E. *Microelectron. Eng.* **2009**, *86*, 1085−1088.

(21) Blossey, R. *Nat. Mater.* **2003**, *2*, 301−306.

(22) McHale, G.; Shirtcliffe, N. J.; Newton, M. I. *Analyst* **2004**, *129*, 284−287.

(23) De Angelis, F.; Gentile, F.; Mecarini, F.; Das, G.; Moretti, M.; Candeloro, P.; Coluccio, M. L.; Cojoc, G.; Accardo, A.; Liberale, C.; Zaccaria, R. P.; Perozziello, G.; Tirinato, L.; Toma, A.; Cuda, G.; Cingolani, R.; Di Fabrizio, E. *Nat. Photonics* **2011**, *5*, 682−687.

(24) Shafrin, E. G.; Zisman, W. A. In *Contact Angle, Wettability and Adhesion Advances in Chemistry Series*; Fowkes, F. M., Ed.; American Chemical Society: Washington D.C., 1964; pp 145−167.

(25) Lafuma, A.; Quéré, D. *Nat. Mater.* **2003**, *2*, 457−460.

(26) Wenzel, R. N. *Ind. Eng. Chem.* **1936**, *28*, 988−994.

(27) Cassie, A. B. D.; Baxter, S. *Trans. Faraday Soc.* **1944**, *40*, 546−551.

(28) Bico, J.; Thiele, U.; Quéré, D. *Colloids Surf., A* **2002**, *206*, 41−46.

(29) Patankar, N. A. *Langmuir* **2004**, *20*, 7097−7102.

(30) Nosonovsky, M.; Bhushan, B. J. *Phys. Condens. Matter* **2008**, *20*, 395005−395011.

(31) Conway, J. H.; Sloane, N. J. A. In *Sphere Packings, Lattices and Groups*; Springer-Verlag Inc.: New York, 1993.

(32) Mahadevan, L.; Pomeau, Y. *Phys. Fluids* **1999**, *11*, 2449.

(33) Dussan, E. B.; Chow, R. T-P. *J. Fluid Mech.* **1983**, *137*, 1−29.

(34) Quéré, D.; Lafuma, A.; Bico, J. *Nanotechnology* **2003**, *14*, 1109−1112.

(35) Kusumaatmaja, H.; Blow, M. L.; Dupuis, A.; Yeomans, J. M. *Europhys. Lett.* **2008**, *81*, 36003−36006.

(36) Moulinet, S.; Bartolo, D. *Eur. Phys. J. E* **2007**, *24*, 251−260.

(37) Reyssat, M.; Yeomans, J. M.; Quéré, D. *Europhys. Lett.* **2008**, *81*, 26006−11.

(38) Deegan, R. D.; Bakajin, O.; Dupont, T. F.; Huber, G.; Nagel, S. R.; Witten, T. A. *Nature* **1997**, *389*, 827−829.

(39) Deegan, R. D.; Bakajin, O.; Dupont, T. F.; Huber, G.; Nagel, S. R.; Witten, T. A. *Phys. Rev. E* **2000**, *62*, 756−765.

(40) Garcia, F. J. V.; Pendry, J. B. *Phys. Rev. Lett.* **1996**, *77* (6), 1163−1166.

(41) Xu, F.; Zhang, Y.; Sun, Y.; Shi, Y.; Wen, Z.; Li, Z. *J. Phys. Chem. C* **2011**, *115*, 9977−9983.